CORRECTED 1 MARCH 2021; SEE FULL TEXT
SCIENCE ROBOTICS | RESEARCH ARTICLE

SOFT ROBOTS

Electro-pneumatic pumps for soft robotics

R. S. Diteesawat[1,2], T. Helps[1,2], M. Taghavi[1,2], J. Rossiter[1,2]*

Soft robotics has applications in myriad fields from assistive wearables to autonomous exploration. Now, the portability and the performance of many devices are limited by their associated pneumatic energy source, requiring either large, heavy pressure vessels or noisy, inefficient air pumps. Here, we present a lightweight, flexible, electro-pneumatic pump (EPP), which can silently control volume and pressure, enabling portable, local energy provision for soft robots, overcoming the limitations of existing pneumatic power sources. The EPP is actuated using dielectric fluid–amplified electrostatic zipping, and the device presented here can exert pressures up to 2.34 kilopascals and deliver volumetric flow rates up to 161 milliliters per minute and under 0.5 watts of power, despite only having a thickness of 1.1 millimeters and weight of 5.3 grams. An EPP was able to drive a typical soft robotic actuator to achieve a maximum contraction change of 32.40% and actuation velocity of 54.43% per second. We highlight the versatility of this technology by presenting three EPP-driven embodiments: an antagonistic mechanism, an arm-flexing wearable robotic device, and a continuous-pumping system. This work shows the wide applicability of the EPP to enable advanced wearable assistive devices and lightweight, mobile, multifunctional robots.

INTRODUCTION

Soft robotics is an emerging field, which may have wide impact across healthcare, industrial, and robotic sectors (*1*–*3*). Many soft robotic devices use pneumatic artificial muscles to exert forces and do work, due to their inherent compliance, low weight, and high actuation speed. Applications include soft actuators (*4*–*10*); wearable assistive devices (*11*–*15*); robot grippers (*16*, *17*); soft manipulators (*18*, *19*); smart skins (*20*, *21*); and locomotion (*22*), navigation (*23*), and entirely soft-bodied (*24*) robots.

Pneumatic artificial muscles exert high forces while contracting or extending under air pressure. However, their applications are limited by their associated large, heavy, and noisy air supplies, which fundamentally limit their portability and performance (*25*–*28*). Conventional electromagnetic (motor-driven) pumps can be used, but these are bulky and rigid. A range of unconventional pumps have been developed as active air sources to address these issues, exploiting non-electromagnetic methods to generate air pressure. Dielectric elastomer pumps (*29*–*31*) have been shown to pump fluids; however, these use rigid frames, which limits their flexibility and suitability for soft robotics applications. Recently, a stretchable electrohydrodynamic pump capable of pumping liquid (*32*), a soft combustion-driven pump (*33*), and a soft pneumatic pump activated using low-boiling point fluids (*34*) were developed to drive soft actuators; however, limitations remain in terms of maximum flow rate [6 ml/min (*32*) and 38.5 ml/min (*33*)] and electrical power consumption [145 kW m^{-3} (*32*)].

Dielectric fluid actuators, such as electro-ribbon actuators (*35*) and hydraulically amplified self-healing electrostatic (HASEL) actuators (*36*, *37*), have recently been developed, which exploit the electrical and hydraulic properties of a dielectric liquid. In these devices, the dielectric liquid amplifies the electrostatic force of attraction between two electrodes, resulting in high-performance actuation. HASEL actuators encapsulate the dielectric liquid within the actuator and exhibit high stress up to 0.3 MPa for standard actuators and up to 6 MPa for Peano-HASEL actuators (*38*). Electro-ribbon actuators are zipping structures that only require a tiny droplet of dielectric liquid at the point(s) where the two electrodes are closest, reducing total actuator mass. When electrically charged, the two electrodes progressively zip together, in a process known as dielectrophoretic liquid zipping (DLZ), resulting in high-contraction (>99%) actuation.

Here, we introduce the electro-pneumatic pump (EPP), a flexible, high-performance pneumatic pump driven by DLZ actuation that overcomes the limitations of conventional electromagnetic pneumatic power sources, generating higher air flow rate and consuming less power. We evaluate the pressure-generating capabilities of the EPP and its behavior when driving a typical pneumatic actuator. We demonstrate a range of EPP applications (antagonistic actuation, a wearable robotic device for the arm, and a continuous-pumping system) showing the EPP's versatility and potential to be used as a silent, lightweight, fast-response pump. These characteristics endow the EPP with the potential to have an effect across robotics and to enable a new generation of entirely soft robots.

RESULTS

EPP concept

The EPP is an active air-transferring device driven by electrostatic zipping. It consists of a flexible air-filled pouch with a pair of electrodes integrated into its sides. These electrodes form a zipping structure, which, upon electrical stimulation, acts to reduce the volume of the pouch and thereby generate pressure (Fig. 1A).

The EPP is fabricated using two identical pouch sides (as shown in Fig. 1D), each comprising an insulated electrode, backing material, and outer pouch wall. The pouch sides are then heat-sealed around their edges to form a sealed pouch (Fig. 1B). The pouch is typically larger than the electrodes in at least one direction, allowing the actuator to expand when filled with air. An air connector is added to one side of the EPP to permit air flow into and out of the actuator. The EPP is flexible and can be easily bent as shown in Fig. 1C. The facile structure of the EPP allows simple, low-cost fabrication of a wide variety of functional soft pumps.

[1]Department of Engineering Mathematics, University of Bristol, Bristol BS8 1BU, UK.
[2]Bristol Robotics Laboratory, Bristol BS16 1QY, UK.
*Corresponding author. Email: jonathan.rossiter@bristol.ac.uk

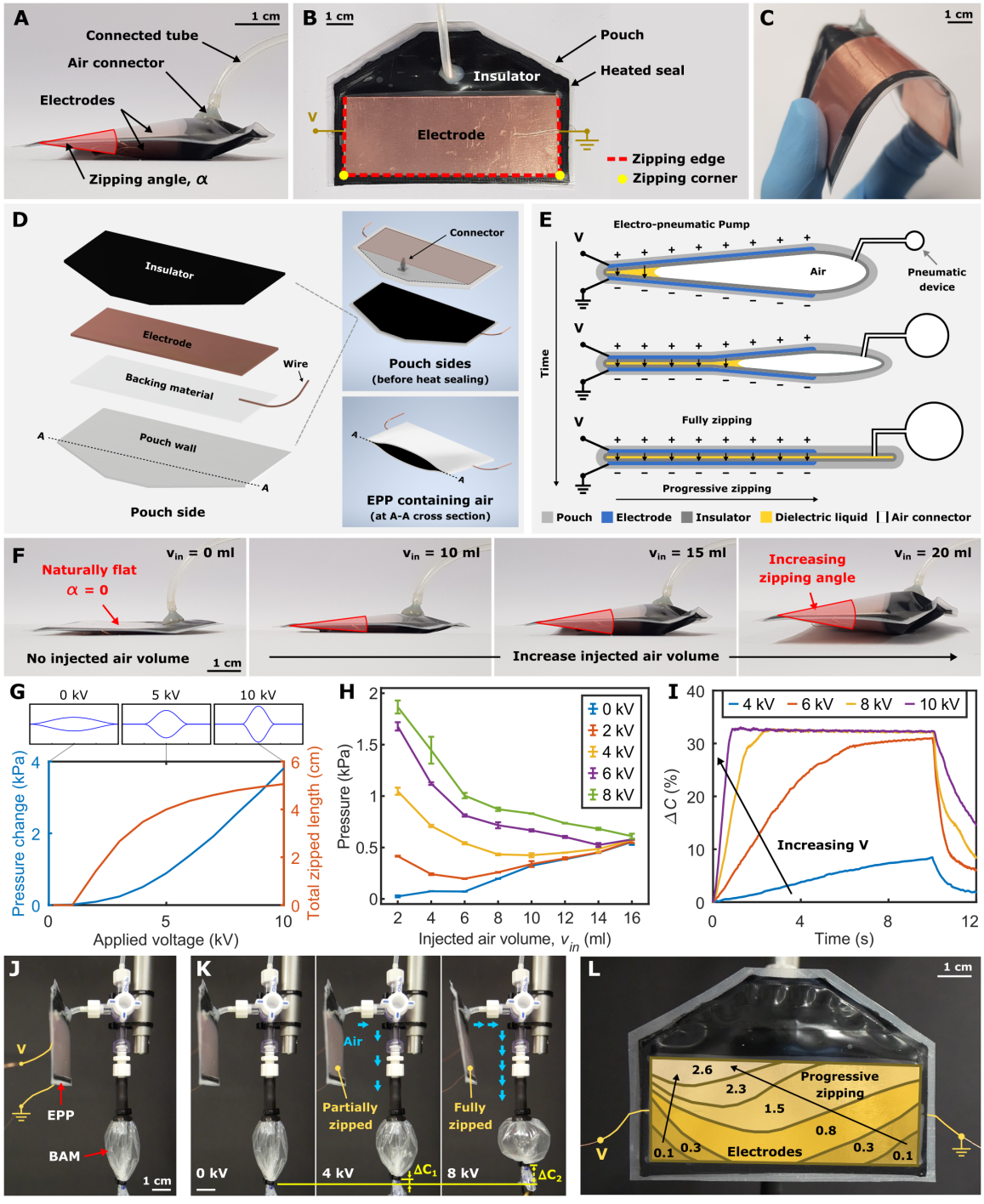

Fig. 1. Principal concepts and actuation of EPP. Photographs showing (**A**) the inflated EPP, (**B**) terminology describing zipping components, and (**C**) flexibility of the EPP. (**D**) Exploded-view schematic diagram showing components and cross-sectional view of the EPP at electrode end. (**E**) Conceptual diagram of DLZ used in the EPP. (**F**) Photographs of the EPP containing different injected air volumes. (**G**) Simulation result of a typical EPP showing the increase in pressure change and total zipped length as voltage is increased (see the Supplementary Materials). (**H**) Capability of the EPP made of 8 cm by 3 cm electrodes in generating pressure while containing different injected air volumes and actuated at different voltages, showing the relationship between pressure and injected air volume. Points are averages of three trials, and error bars show ±1 SD. (**I**) Contraction change Δ*C* of a connected pneumatic actuator (BAM) actuated by the EPP at different voltages. (**J**) Photograph of the EPP connected to the BAM. (**K**) Actuation of the EPP-BAM system at 0, 4, and 8 kV (blue arrows denote the amount of air volume transferred from the EPP to the BAM). (**L**) Progressive zipping of the EPP actuated at 8 kV (numbers indicate time in seconds).

A typical EPP is made using electrodes of dimensions 8 cm by 3 cm. Actuation of the EPP is defined by three adjacent zipping edges and two zipping corners, where the zipping edges meet (Fig. 1B). The zipping angle (α) defines the angle between two electrodes (Fig. 1A). In its fabricated state, the EPP has zero internal volume and $\alpha = 0$ (Fig. 1F). For the EPP to actuate, α must be greater than zero, and it must contain an internal air volume. To achieve this, air must be injected into the EPP. The injected air volume (v_{in}) refers to the volume of air at atmosphere pressure (P_{atm}) and at room temperature that is injected into the pneumatic system. As the EPP is inflated (increasing v_{in}), it deforms and α increases (Fig. 1F). As v_{in} increases, the pressure and volume of the whole pneumatic system changes because air is compressible. Initial pressure, P_i, is the pressure of the system with no EPP actuation (0 kV), and actuated pressure, P_a (V), is the pressure at applied voltage V. The addition of two check valves allows the EPP to pump air continuously.

EPP actuation uses the concept of DLZ (*35*) in a closed system: The electrodes are oppositely charged, and the small droplet of liquid dielectric contained inside the pouch amplifies electrostatic force, allowing for high-force, progressive electrostatic zipping that acts to close the pouch and transfers compressed air to a connected pneumatic device (Fig. 1E). This electrostatic force decreases monotonically as zipping angle α increases. Figure 1G shows electrostatic zipping and the resultant increase in pressure as the applied voltage is increased in a mathematical model of an EPP system. The mathematical model is provided in the Supplementary Materials.

To evaluate the fundamental characteristics of the EPP, a typical EPP was fabricated without check valves and tested to characterize its pressure-generating capabilities (as shown in fig. S5). When increasing v_{in}, initial pressure (P_i) increased, while actuated pressure (P_a) decreased, causing reduction of ΔP, the difference between P_a and P_i ($\Delta P = P_a - P_i$), as shown in Fig. 1H and fig. S4.

At low v_{in}, the EPP fully zipped ($\alpha \rightarrow 0$), resulting in a strong electrostatic force and associated high-pressure generation. In contrast, at high v_{in}, the EPP partially zipped because the larger air volume resisted compression, resulting in a larger zipping angle and lower electrostatic force. Further increasing v_{in} prevented the EPP from zipping.

To demonstrate the efficacy of the EPP in transferring air, it was used to actuate a typical pneumatic contractile actuator, a bubble artificial muscle (BAM) (*5*, *6*) derived from the series pneumatic actuator (*7*), which was made from 30-μm-thick, 17-mm-radius plastic tubing that had a length of 40 mm and an unactuated radius of 3 mm, loaded with an external mass of 26.5 g. The EPP was connected through a three-way valve to the BAM and a syringe, allowing for control of initial air volume (v_{in}) (Fig. 1J). BAM contraction (C) is defined as actuator length subtracted from extended length, divided by extended length, expressed as a percentage. C is equal to 0% at no inflation (full extension). Initial contraction (C_i) is the BAM contraction at no EPP actuation (0 kV) and pressure P_i. Actuated contraction (C_a) is the BAM contraction at applied voltage V and pressure $P_a(V)$, where $0 \leq C_i \leq C_a$. Contraction change ΔC is the difference between C_a and C_i ($\Delta C = C_a - C_i$). As voltage applied to the EPP increased, ΔC increased up to a maximum of 32.40%. Full zipping of the EPP occurred at a voltage of 8 kV (Fig. 1, I and K).

When a voltage is applied, the EPP starts zipping from the zipping corners, which have the shortest distance between two electrodes, resulting in the highest electric field. As the EPP zips, the dielectric liquid is squeezed along in the same direction such that it is always coincident with the zipping point. This ensures that it amplifies electrostatic force as the EPP progressively zips (Fig. 1L). BAM contraction and EPP zipping are shown in movie S1.

Characterization of combined EPP and BAM system

The previously described BAM was used to evaluate the performance of the EPP in an isotonic experimental setup (fig. S5). Actuation of the BAM under different loads is shown in fig. S6. Various air volumes (v_{in}) were injected into the EPP-BAM system, and a voltage of 8 kV was applied to the EPP (8 cm by 3 cm). At a given voltage, the maximum amount of zipping in the EPP and the maximum contraction change (ΔC) of the BAM were dependent upon v_{in} (Fig. 2A). For each load, there was a v_{in} that maximized actuated contraction C_a (Fig. 2B). Below this v_{in}, the EPP fully zipped but did not displace enough air to maximally contract the BAM. Above this v_{in}, the injected air resisted EPP actuation, as in the case of the EPP pressure experiments (Fig. 1H). This resulted in less displaced air and lower ΔC. This behavior of the EPP-BAM system can be observed in movie S2. At 8-kV EPP actuation, the BAM delivered ΔC of 31.48, 29.05, and 18.29% under loads of 26.5, 50.2, and 100.4 g, respectively (Fig. 2B). Both maximum C_a and the injected air v_{in} at which C_a was maximized decreased with increasing load.

The EPP-BAM system with an external load of 26.5 g, containing v_{in} of 17 ml (the injected air volume that maximized ΔC at this load), was studied further to observe change in BAM contraction, pressure of the EPP-BAM system, and BAM actuation velocity at different voltages (Fig. 2C). BAM contraction started at 4 kV and reached a maximum at 7 kV, whereas the actuation velocity continuously increased with applied voltage as electrostatic force increased (movie S3). The BAM actuated by the EPP at different voltages showed the same contraction-pressure relationship as that of a syringe-actuated BAM (Fig. 2D). The variation between three EPP-BAM systems featuring different EPPs with the same electrode dimensions is shown in Fig. 2E.

EPP design characterization

To explore the effect of different designs on the performance of the EPP, three additional EPP designs with different dimensions were fabricated without check valves and tested (varying electrode length and width while conserving total electrode area). We refer to these EPP designs as D2, D3, and D4; the EPP design previously presented is D1 (Fig. 3A and table S1). These four EPPs have different zipping edge lengths but have similar weights (4.9 to 5.3 g). The volume of dielectric liquid injected into each EPP was kept to a minimum and was between 1 and 2% of the maximum volume of the EPPs (table S1). The inflation stiffness of each EPP design is different due to their different geometry, as can be observed by the change of initial pressure (P_i) when inflating them with a certain v_{in} (Fig. 3B). EPP stiffness increases from D1 to D4.

The actuated pressure changes (ΔP) of these four EPPs are illustrated in Fig. 3C. Higher applied voltage resulted in higher pressure. The maximum ΔP occurred when the EPPs contained low v_{in} and almost fully zipped, except for EPP D3, for which there was intermediate v_{in} that maximized ΔP. We attribute this to buckling and creasing effects associated with this design. ΔP decreased with increasing v_{in} and reduced to zero at different v_{in} for different designs. EPP D4 generated the highest ΔP of 2.34 kPa (Fig. 3C). In contrast, EPP D2 delivered the highest peak-specific energy, energy density, specific power, and power density of 2.59 J/kg, 356.68 J/m^3, 112.16 W/kg, and 15.46 kW/m^3, respectively (fig. S8).

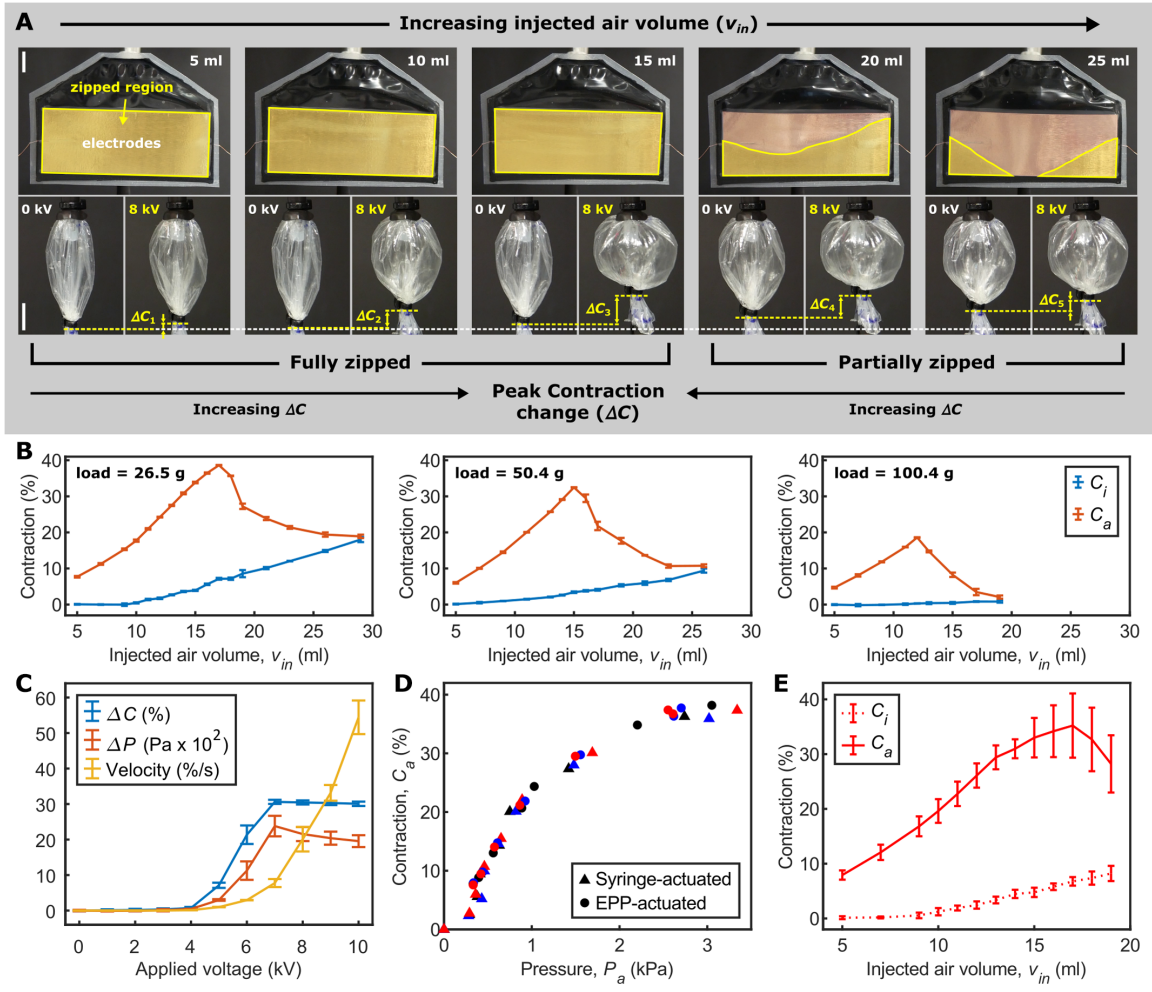

Fig. 2. Actuation characterization of the EPP-BAM system. (**A**) Zipping behavior when increasing v_{in}, showing maximally zipped state and contraction change when actuated at 8 kV. Photographs of the EPP show the zipped region of the electrodes at 8 kV in yellow and the BAM at 0 kV (C_i) and 8 kV (C_a). The white dashed line shows the initial contraction C_i of the BAM at v_{in} = 5 ml and 0 kV; yellow dashed lines show contraction change ΔC of the BAM at different v_{in}. Scale bars, 1 cm. (**B**) Initial and actuated contractions at different v_{in} under different applied loads. (**C**) Contraction change ΔC, pressure change ΔP, and actuation velocity of the BAM under a load of 26.5 g when v_{in} = 17 ml, actuated at increasing applied voltages. (**D**) Comparison of syringe-actuated and EPP-actuated BAM (different colors indicate different experimental trials). (**E**) Sample variation of BAM contraction when actuated by three EPPs of the same dimensions. In (B) and (C), points are averages of three trials and error bars show ±1 SD. In (E), points are averages of three trials from three EPPs (nine trials total), and error bars show ±1 SD.

Figure 3D shows key performance metrics of each EPP when actuating the previously described BAM under loads of 26.5, 50.2, and 100.4 g at V = 8 kV. For each design, the v_{in} that maximized C_a was used. When increasing v_{in} at 0 kV, the BAM connected to the stiffest EPP, D4, had a larger initial contraction (C_i) compared with the BAM connected to the softest EPP, D1 (Fig. 3E), because the stiffer EPP implies a lower ratio of injected air between EPP and BAM. When the EPP is stiffer than the BAM, most of v_{in} will remain in the BAM. When the load was increased, more air was pushed into the EPP, reducing C_i (Fig. 3F).

EPP D1 was found to produce the highest contraction change, ΔC, among all EPPs and loads tested (Fig. 3, D and G). EPPs require very low currents to deliver actuation; maximum current draw for all EPPs was less than 100 μA, and continuous current draw in their actuated state (while maintaining pressure) was less than 20 μA at 8 kV (Fig. 3D), implying low power consumption less than 0.16 W. Efficiency was calculated by dividing mechanical output power by electrical power consumed; EPP D4 had the highest peak efficiency of 46.5% (fig. S8).

EPP-BAM capabilities

Experiments were performed to demonstrate the versatility of this novel soft pump. EPP D1 was connected to the previously described BAM, loaded with a mass of 26.5 g. The EPP-BAM system contained v_{in} = 15 ml, and the EPP was actuated at different frequencies between 0.1 and 2.0 Hz at V = 8 kV (Fig. 4A and movie S4). The highest frequency that allowed for full contraction of the BAM was 0.2 Hz; the interpolated −3-dB cutoff frequency was at 0.38 Hz (Fig. 4B).

Voltage control of EPP-BAM systems is also possible; Fig. 4C shows EPP D1 holding the BAM at various intermediate contractions, reachable by adjusting voltage. To increase and decrease BAM contraction, voltages of 8 and 1 kV, respectively, were applied momentarily. To hold BAM at different C_a, a holding voltage in the

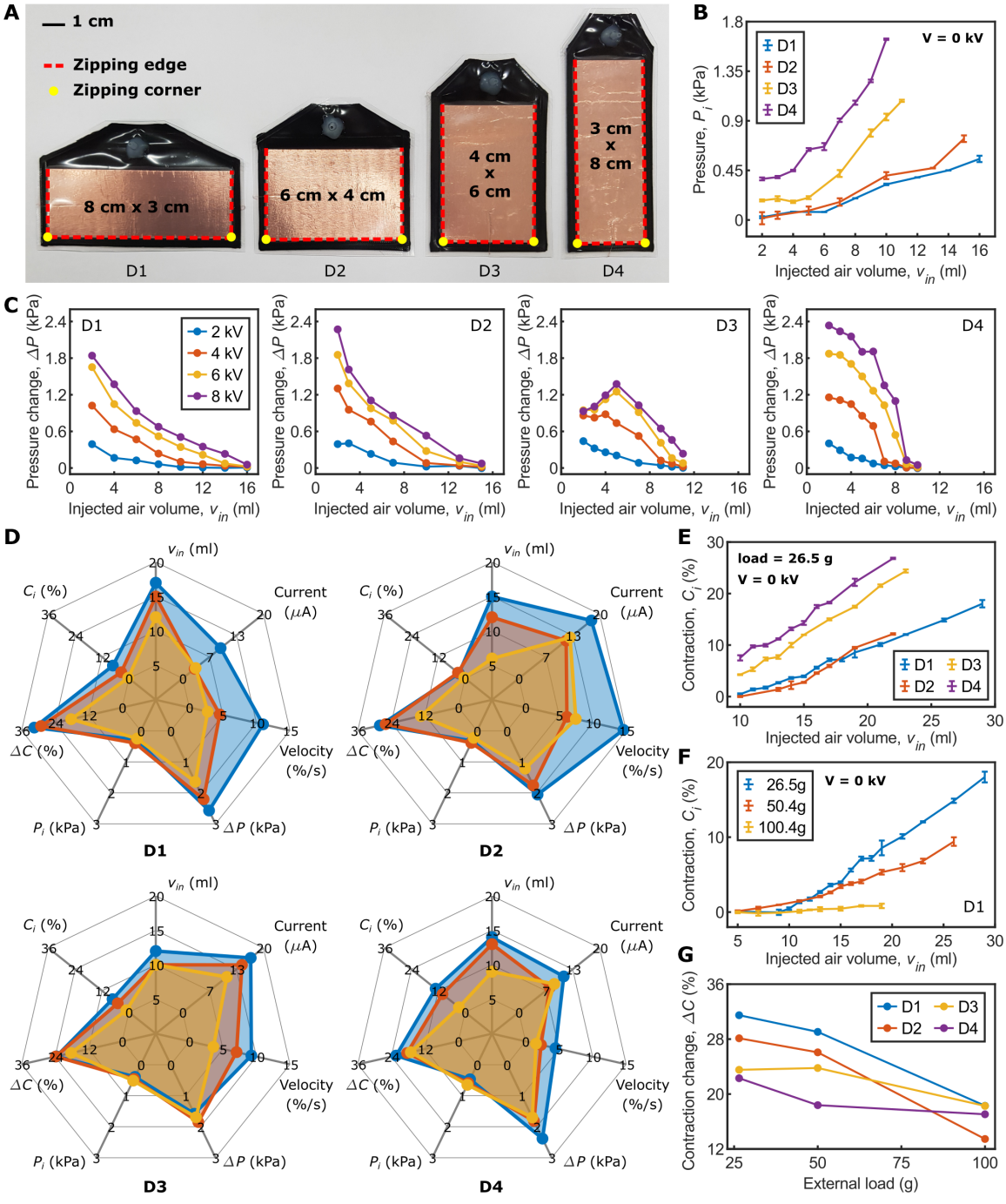

Fig. 3. Design characterization of the EPP and the EPP-BAM system. (**A**) Photographs of four EPP designs with different dimensions. (**B**) Initial pressure P_i of the four EPPs when increasing v_{in}. (**C**) Pressure change ΔP of the four EPPs directly connected to the pressure sensor, actuated at different voltages. (**D**) Spider plots of each EPP design's key performance metrics when actuating a BAM under different loads at an applied voltage of 8 kV. Loads were 26.5 g (blue area), 50.2 g (red area), and 100.4 g (yellow area). Current describes the continuous current draw of the EPP when in its actuated state (while maintaining pressure). Velocity describes the average velocity of the BAM during contraction. (**E** and **F**) Initial contraction C_i of the BAM connected to (E) each EPP when loaded with a 26.5-g mass or (F) EPP D1 when loaded with different masses. $V = 0$ kV in (E) and (F). (**G**) Contraction change ΔC of the EPP-BAM system under different loads. In (B), (E), and (F), points are averages of three trials and error bars show ±1 SD.

range of 3.7 to 4.7 kV was applied depending on the amount of contraction. This provides a promising possibility for the EPP pump to be readily controllable. An example of the EPP control can be found in movie S5.

Cyclic testing was undertaken over 10,000 cycles at a frequency of 1 Hz (Fig. 4D). EPP D1 was actuated at a voltage of 8 kV, whereas the BAM was loaded with a mass of 70 g. The EPP-BAM system contained v_{in} of 7 ml, less than in the experiments for Fig. 4A, to

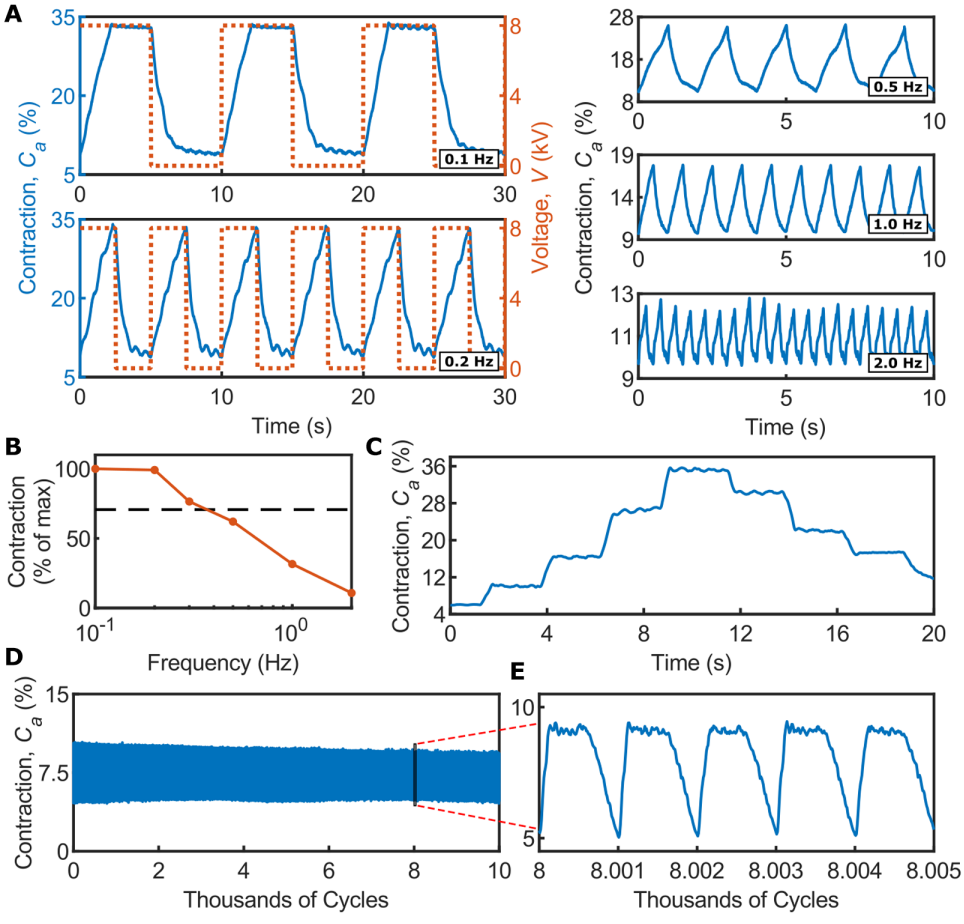

Fig. 4. Capabilities of the EPP-BAM system (EPP D1). (**A**) Actuation at frequencies of 0.1, 0.2, 0.5, 1.0, and 2.0 Hz at $V = 8$ kV. (**B**) Bode plot of actuator frequency response at $V = 8$ kV (dashed line indicates −3 dB). (**C**) Voltage control allowing the EPP to hold the BAM at different intermediate contraction values. (**D**) Cyclic test of the EPP-BAM system, over 10,000 cycles at a frequency of 1 Hz and at voltage of 8 kV. (**E**) Five actuation cycles after 8000 cycles.

enable full zipping at 1-Hz actuation. After 8000 cycles, the contraction change (ΔC) reduced by 1.17% (Fig. 4E).

EPP for soft robotics applications

Experiments were undertaken to demonstrate the suitability of the EPP for use in real-world applications. Using a pair of EPP-BAM systems (of D1) allows for an antagonistic mechanism, connecting each end of the BAMs to a connecting bar (Fig. 5A). The EPPs were actuated with a 180° out-of-phase square wave at a range of frequencies. The system moved the connecting bar at frequencies up to 5 Hz (movie S6).

An arm-flexing wearable robotic device was designed as shown in Fig. 5B. The device consisted of two EPPs (D1) connected in parallel, a BAM with three contractile units (total length of 11.5 cm, unactuated radius of 2 mm), and a plastic skeleton arm to represent a human arm. Both EPPs were actuated simultaneously, causing the BAM to contract and the forearm (mass of 18.62 g) to lift. A maximum stroke of 23.0 cm was achieved at v_{in} = 40 ml (Fig. 5, C to F, and movie S7). When deactivating the EPPs, the arm lowered due to gravity; an antagonistic mechanism for both flexion and extension could be applied to the arm to increase the speed at which the arm lowered. The wearable robotic device was able to deliver strokes up to 15.1 cm and 9.6 cm, while the arm was loaded with a 4.8-g toy duck and a 20-g mass, respectively (Fig. 5, G to J).

A continuous-pumping system was fabricated by inserting a sponge between the two electrodes at the center of an EPP (D1, Fig. 6A). This sponge acts as a soft spring, generating a restoring force to open the EPP at 0 kV. In previous experiments, the restoring force was provided by the compressed air within the system and additionally the external load in the case of the EPP-BAM system. The EPP was connected to two one-way valves for passive control of air input and output, enabling continuous pumping. Two experimental setups were used to evaluate the flow rate at atmospheric pressure (P_{atm}) and at output pressure higher than P_{atm}, as shown in Fig. 6A and fig. S9A, respectively. In the first experimental setup (P_{atm}), the EPP pump was connected to a volume measurement setup comprising a water trough and an inverted 10-ml measuring cylinder (Fig. 6A). The EPP was actuated at an applied voltage of 10 kV at different frequencies. Two experiments were undertaken using this setup. In the first experiment, pumped air volume after two cycles was recorded (Fig. 6, B and C). In the second experiment, flow rate was calculated during 2 s of actuation (Fig. 6, D to F, and movie S8). When actuating the EPP pump for two cycles, the pumped air volume decreased with increasing frequency (Fig. 6C). When actuating the EPP pump for 2 s, the EPP flow rate was maximized first at 2.65 ml/s at 2 Hz. Its flow rate slightly reduced when frequency was increased, until approaching a second peak of 2.68 ml/s at 25 Hz (Fig. 6D). The high flow rate achieved at high frequency and associated small EPP contractions suggests the possibility of creating an extremely small EPP pump that retains the high performance of the EPP demonstrated here. In the second experimental setup, output flow rate was measured using a flow rate sensor as back pressure (setup varying the height of water above the output) was varied (fig. S9A). The EPP exhibited lower flow rates as output back pressure was increased, and flow rate was maximum at 5 Hz (fig. S9, B and C), consistent with the first pumping experiment (at P_{atm}). When output pressure was higher than P_{atm}, flow rate reduced considerably above 20 Hz. Figure 6G shows the relationship between flow rate and pressure at different frequencies. Average electrical power consumption decreased with higher pressure but increased with higher frequency (fig. S9D). This is because the EPP zipped more at low pressure, resulting in higher current consumption. The initial region of zipping required the highest current consumption to rapidly charge the electrodes; thus, actuation at high frequency (with more charging cycles) increased power consumption.

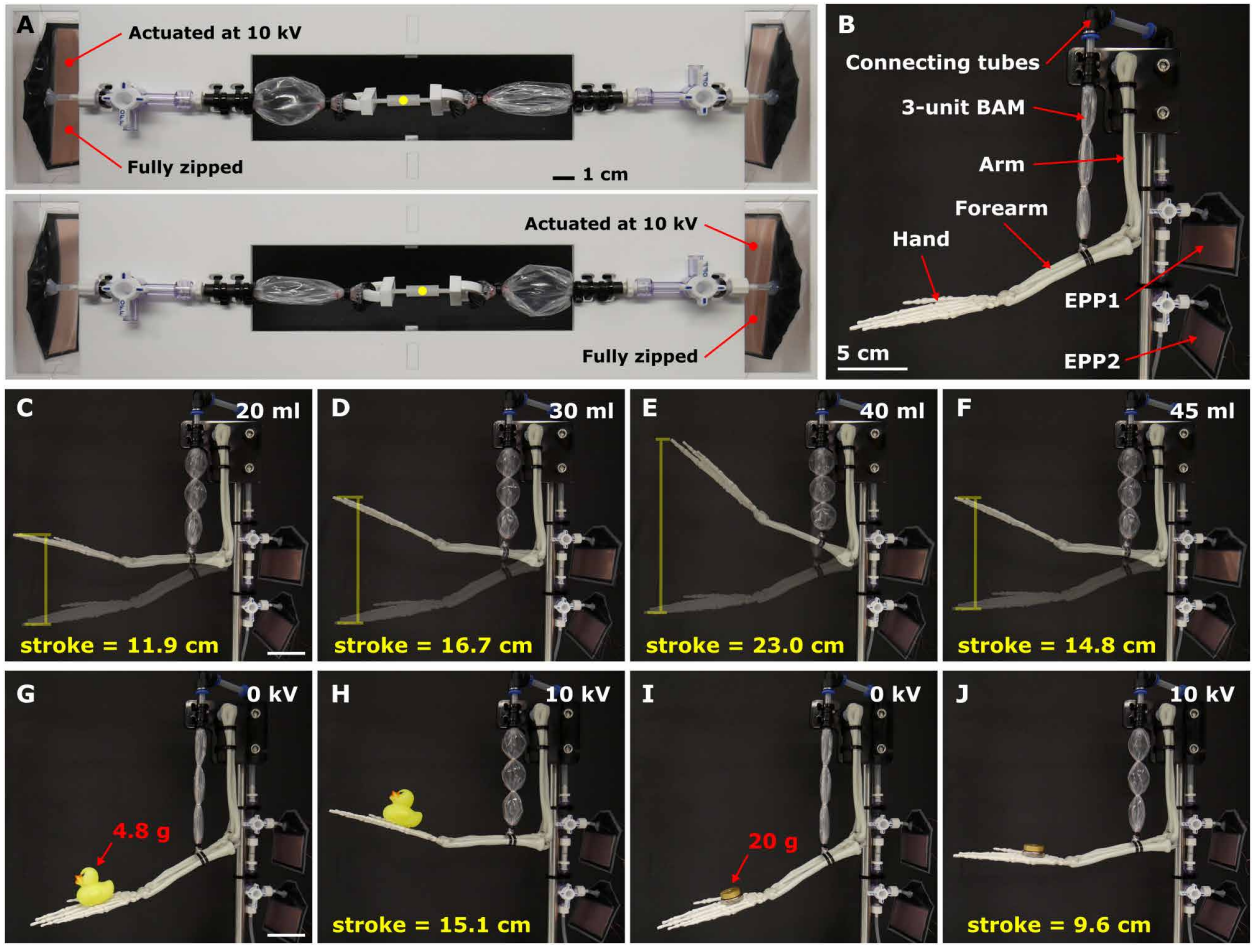

Fig. 5. EPP-BAM antagonistic mechanism and arm-flexing wearable robotic device. (**A**) Antagonistic mechanism featuring two identical EPP-BAM systems (EPP D1) connected in parallel, actuated at 10 kV (yellow dots indicate the center of the connecting bar). (**B**) Experimental setup of the wearable robotic device, driven by two parallel EPPs (D1). (**C** to **F**) Motion of the arm when actuated at 10 kV, but with different v_{in} for the EPP-BAM system of 20, 30, 40, and 45 ml, respectively. (**G** to **J**) Resting and actuation states of the arm while holding a 4.8-g toy duck (G and H) and a 20-g load (I and J).

To demonstrate the flexibility of the EPP, pressure change ΔP was recorded for a bent EPP of D1 (fig. S10). With increasing bending, initial pressure P_i increased, whereas pressure change ΔP reduced when actuated (fig. S10B). Actuation at lower frequency allowed the EPP to zip more, resulting in larger pressure generation. Figure S10C shows pressure change over time for an unbent and bent EPP at frequencies of 0.2, 0.5, and 1.0 Hz.

DISCUSSION

We have presented the EPP, a lightweight, flexible device capable of generating pressure and transferring air when electrically charged. Its stiffness depends on its geometry and the materials used in its fabrication; stiff EPPs generated high pressure, whereas soft EPPs transfer high air volumes. EPP maximum pressure change was 2.34 kPa (specific and density values are 0.472 MPa kg^{-1} and 78.7 MPa m^{-3}, respectively), lower than the 14 kPa delivered by the stretchable pump presented in (*32*); however, the EPP is capable of pumping air rather than liquid, making it suitable for driving pneumatic artificial muscles.

The highest continuous-pumping air flow rate demonstrated here was 2.68 ml/s (161 ml min^{-1}). It exhibits a high specific flow rate (30.5 liters min^{-1} kg^{-1}), comparing favorably with that of the stretchable pump (~4 liters min^{-1} kg^{-1}). Its flow rate density (4.59 kl min^{-1} m^{-3}) was similar to that of the stretchable pump (5.13 kl min^{-1} m^{-3}) and the combustion-driven pump (0.82 kl min^{-1} m^{-3}) presented in (*33*).

The EPP exhibits extremely low power consumption (less than 0.53 W or 15.0 kW m^{-3}), lower than that of the stretchable pump (145 kW m^{-3}) and considerably lower than that of a commercial electromagnetic miniature pump [512 kW m^{-3}, MGD 1000S (*39*)] with a similar flow rate density (8.5 kl min^{-1} m^{-3}). EPP D4 exhibited the highest peak efficiency of 46.5%.

The EPP-BAM system delivered a maximum ΔC of 32.4% (load, 26.5 g) and lifted a maximum load of 100.4 g (corresponding to 0.98 N), which compares favorably with the maximum ΔC of 2.2% and the maximum blocking force of 0.84 N reported for thin McKibben muscles actuated by the stretchable pump (*40*). Its maximum actuation velocity was 54.43%/s at 10 kV (Fig. 2C). Voltage control experiments with the EPP-BAM system suggest that it is readily controllable, enabling applications where precise pumping behavior is required.

Although the EPP is driven by high voltage, no conductors are exposed to the outside of the pump other than insulated wires,

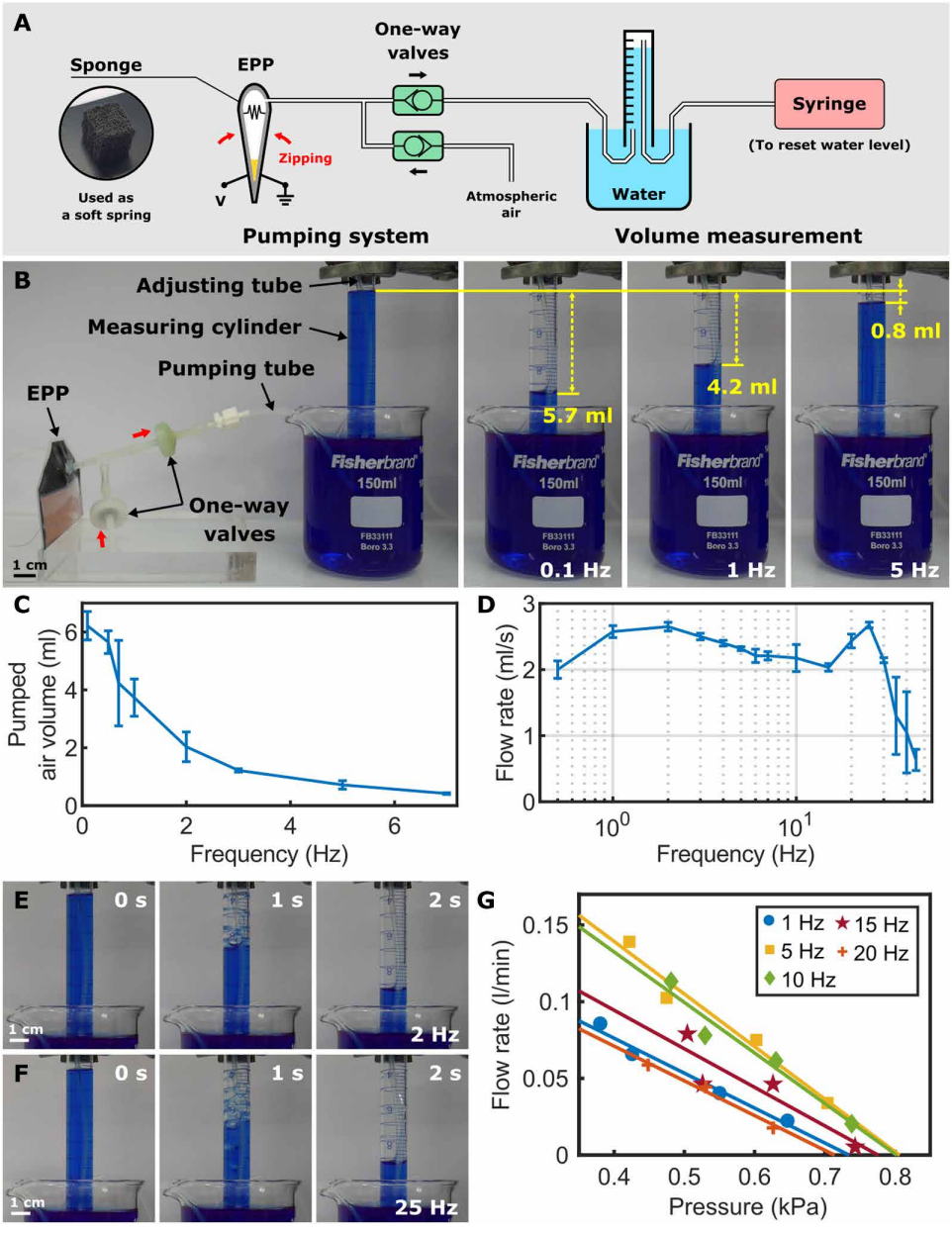

Fig. 6. Continuous pumping using EPP D1. (**A**) Experimental design to measure flow rate at atmospheric pressure (P_{atm}). (**B** and **C**) Variation in pumped air volume during two actuation cycles at different frequencies at P_{atm}. (**D**) Variation in average flow rate during 2 s of cyclic actuation at different actuation frequencies at P_{atm}. (**E** and **F**) Variation in pumped air volume over 2 s of cyclic actuation at actuation frequencies of 2 and 25 Hz, respectively. In (C) and (D), points are averages of three trials, and error bars show ±1 SD. (**G**) Relationship between mean flow rate and mean pressure (across three trials) of the EPP pump when setting output pressure higher than P_{atm}, actuated at frequency between 1 and 20 Hz (experimental data are presented as markers, also shown are linear best-fit lines of the data for each frequency).

which limits the possibility of exposure to high voltage. Furthermore, the maximum current delivered to the EPPs demonstrated here was less than 100 μA, considerably lower than the 20-mA maximum permitted by Underwriters Laboratories and International Electrotechnical Commission consumer electronics safety standards (*41*).

EPPs can be used as a portable pump for soft robotics when paired with a miniature portable high-voltage supply as in (*32*), which has a mass of only 20 g, demonstrating their potential for wearable robotics applications. The EPP-BAM wearable robotic device was able to drive an arm to exert force and do work, suggesting that it can generate useful forces for wearable applications. Although the wearable EPP device was demonstrated lifting a limited weight of 20 g (in addition to the 18.62-g forearm), future wearable devices will integrate cells containing multiple improved EPPs to deliver higher forces. Nonetheless, the wearable EPP device presented here is suitable to low-force wearable applications such as tactile stimulation and touch-based navigation.

To improve the EPP's performance in generating pressure and flow rate, different geometries and actuator designs can be investigated to increase the active zipping region and reduce the inactive region. For example, triangular electrodes whose width increases as zipping propagates could increase electrostatic force as backpressure increases. In the future, the EPP-BAM system will be miniaturized, resulting in a smaller zipping angle, improving zipping effectiveness. For integration into assistive clothing, several miniaturized EPP units can be included in an array, which can be actuated to assist body movement when required. Last, different materials with higher permittivity and electrical breakdown will be explored to improve electrostatic force and actuation performance. In addition, the control schemes and self-sensing of similar dielectric zipping actuators (*42*, *43*) can be implemented in the EPP to improve actuation precision and performance.

The EPP's high performance and versatility demonstrated here show its wide applicability across robotics and autonomous systems. As a flexible, silent, lightweight, and fast-response pump, it has the potential to enable advanced wearable assistive devices and a new generation of entirely soft, mobile, and multifunctional robots.

MATERIALS AND METHODS

Manufacture of EPP

EPPs were fabricated from two identical pouch sides; each side included an insulated electrode, backing material and outer pouch wall (Fig. 1D). Polyvinyl chloride (PVC) tape (130-μm thickness; AT7, Advance Tapes, UK) was used as an insulator. Copper tape

(35-μm thickness; AT525, Advance Tapes, UK) formed the electrode, attached to a 240-μm-thick PVC backing sheet (A4 Clear PVC Covers, Binding Store Ltd., UK). The backing material provided stiffness to the actuator. Electrical connections were made using enameled copper wires (CUL 100/0,15, BLOCK Transformatoren-Elektronik GmbH, Germany). Low-density polyethylene (LDPE; 125-μm thickness) layflat tubing (LFT9500STK, Polybags Ltd., UK) was used as a pouch material, and pouch sides were heat-sealed around their edges, using an impulse heat sealer (HS300C, Polybags Ltd., UK), to form an EPP. A $^{1}/_{16}$-inch-diameter polypropylene straight connector (#06365-11, Cole Parmer, UK) was attached to one side of the pouch by hot glue. A drop of silicone oil (#317667, Sigma-Aldrich, USA) was injected into the pouch to act as the dielectric liquid. The total thickness of the empty EPP was 1.10 mm. For the continuous-pumping system (Fig. 6), a sponge with dimensions 10 mm by 10 mm by 12 mm (103-4073, RS Components Ltd., UK) was inserted into the EPP before final sealing.

The improvement of electrostatic force in dielectric zipping actuators using different materials has been investigated in (*44*), suggesting that materials with high permittivity are preferred and that the insulator permittivity should be higher than the medium permittivity. Consequently, silicone oil and PVC tape were selected to be used as dielectric liquid and insulator due to their high permittivity and electrical breakdown strength, resulting in high electrostatic force amplification. The relative permittivity of silicone oil and PVC tape is 2.7 and 4.62, respectively. Silicone oil has a breakdown strength of 20 MV/m (around 6.7 times greater than that of air), whereas a single layer of the PVC tape used has a breakdown voltage of 8000 V, implying around 60 MV/m given its 130-μm thickness (around 20 times greater than that of air) (*35*).

Manufacture of BAM

BAMs (*5*) were made from 30-μm-thick LDPE layflat tubing (LFT2120STK, Polybags Ltd., UK) as an actuator membrane. One actuator end was connected to a polyurethane tube with an outer radius of 3 mm (197377, FESTO, Germany) for air input/output, and heat shrink tubing was used to seal the layflat tubing to the polyurethane tube. The impulse heat sealer was used to seal the other end of the BAM, and both ends were further secured using cable ties. For the BAM used in the wearable robotic device, two metal retaining rings with inner radius of 2 mm (MM Watch Co. Limited, UK) were added to create three series contractile units to increase its total actuation stroke.

Experimental setup

Performance evaluation

Figure S5 shows the experimental setup used to evaluate the performance of the EPP. By changing the position of the three-way valve, three different experiments were conducted: (i) EPP pressure generation (only EPP), (ii) BAM manual inflation (only BAM), and (iii) BAM actuation by the EPP (EPP-BAM system).

First, the EPP was evaluated by measuring the air pressure when a fixed volume of air at atmospheric pressure was injected into the system, and a voltage was applied across the two electrodes. The EPP was connected to a pressure sensor (HSCDANN030PGAA5, Honeywell, USA) to measure internal pressure, and a standard 60-ml syringe was used to inject a known air volume (v_{in}) through the three-way valve (Cole Parmer, UK). The EPP was charged using a 0.68-kg high voltage amplifier (5HVA24-BP1, UltraVolt, USA) at a range of input voltages, controlled by a computer running MATLAB. A National Instruments data acquisition device (NI USB-6343, National Instruments, USA) was used to control the input voltage and to record output data at a sampling frequency of 1000 Hz. Each test was repeated three times.

Second, the contraction-pressure relationship of the BAM was determined by measuring contractile displacement and internal pressure while adjusting v_{in} using the syringe. Different external loads were suspended from the BAM. A laser displacement sensor (LK-G152, Keyence, Japan) was used to measure the displacement of the load. Each test was repeated three times for a range of loads.

Third, the performance of the EPP in inflating the BAM was assessed by connecting the EPP and BAM together. The EPP was actuated, and the pressure of the EPP-BAM system and BAM contraction were recorded. The syringe was used to control v_{in} of the EPP-BAM system. Each experiment was repeated three times at a range of v_{in} and loads.

Arm-flexing robotic device

An arm-flexing robotic device was demonstrated on a skeleton arm model (12.5-cm-long upper arm and 22-cm-long forearm and hand) (Fig. 5B). The BAM was anchored to a rigid mount near the shoulder and to the forearm 4 cm from the elbow. Actuation of the BAM lifted the 18.62-g forearm. v_{in} was adjusted to deliver the highest flexion. The weights of the series BAM and two EPP units were 2.48, 5.72, and 5.82 g, respectively, resulting in total weight of the wearable robotic device of 14.02 g.

Continuous-pumping system

For the continuous-pumping system (Fig. 6 and fig. S9), two one-way valves were connected to the EPP to ensure directional pumping. For actuation at atmospheric pressure P_{atm} (Fig. 6), an outlet tube was set at the same position of water level in a water trough, where output pressure is P_{atm}. Pumped air volume was measured by observing the change in water level in a 10-ml measuring cylinder (#11517832, Fisher Scientific UK Ltd., UK). To evaluate flow rate at different output pressure higher than P_{atm}, a flow rate sensor (AWM510VN, Mass Air Flow Sensor, Honeywell, USA) was connected to the EPP pumping system, and its outlet was connected to a tube through the pressure sensor. This tube was set at different water levels to apply different output pressures, as shown in fig. S9A.

Pressure generation of bent EPP

The continuous-pumping EPP was actuated at its natural shape and increasingly bent shapes (fig. S10A). It was bent by constraining it within a clamp, with clamp length (L_{clamp}) set at 90 (unbent), 75, and 70 mm. It was actuated at different frequencies but a constant maximum applied voltage of 8 kV to generate pressure change ΔP, measured by the pressure sensor.

Data acquisition and analysis

For visualization, all data were smoothed using the MATLAB "smooth" function with span of 0.01 and method of "rloess." In some experiments, the EPP pressure under actuation either increased asymptotic to a stable value or retained a small oscillatory component. In all cases, the average data in the stable region were used as the recorded value.

Actuation simulation of the EPP

Figure 1G shows zipping simulation and pressure generation of an EPP device of similar dimensions to D1 (8-cm-long, 3-cm-wide electrodes) when electrically charged at applied voltages from 0 to

10 kV. It contained an initial internal pressure of 25 Pa and 0.34 ml of silicone oil, as liquid dielectric, to amplify electrostatic force at both zipping corners. The electrostatic pressure and force were derived based from (*35*), and the actuator shape was simulated using Euler-Bernoulli beam theory, assumed as a fixed-fixed beam. An electrical breakdown assumption and zipping detection were also included in this simulation. Because the EPP contained a constant air volume, the ideal gas law was used to calculate the change in pressure due to change in the actuator shape. Full details of the mathematical model and simulation process can be found in Supplementary Materials and Methods and figs. S1 to S3.

Calculation of energy, power, and efficiency

Energy, power, and efficiency are calculated from pressure generation of the EPPs, considered as an isothermal system because the temperature (T) was not observed to change during actuation. Output energy (E_{output}) is a function of $nRT{\cdot}\log(P_A/P_B)$, where n is the amount of gas, R is the ideal gas constant (8.314 J mol^{-1} K^{-1}), and P_A and P_B are the absolute pressure at different states after certain period: initial pressure at no actuation, P_i, and actuated pressure at time t, $P_a(t)$, respectively. The EPP is a closed system containing a constant amount of air, so $n = (P_{atm})(v_{in} + v_{connector})/RT$, where v_{in} and $v_{connector}$ are the injected air volume and volume of the connecting tube between the EPP and the pressure sensor (about 1.5 ml) at atmospheric pressure P_{atm}, respectively. Thus, the equation to calculate E_{output} is

$$E_{output}(t) = (P_{atm})(v_{in} + v_{connector}) \cdot \log\left(\frac{P_i + P_{atm}}{P_a(t) + P_{atm}}\right) \quad (1)$$

Output power (P_{output}) is calculated as the change in output energy over 1 ms, and input power (P_{input}) is the product of applied voltage (V) and current drawn (I) at each millisecond, measured by the high-voltage amplifier and data acquisition device. Input energy (E_{input}) is the definite integral of input power over an actuation time interval from zero to t. Efficiency is calculated as the ratio between P_{output} and P_{input}. Power and efficiency are calculated at every millisecond and reported as peak values.

Specific energy and power of each EPP were calculated by dividing the energy and power with their respective actuator mass, whereas their energy and power density were calculated by dividing the energy and power with their respective maximum actuator volume. The actuator mass and maximum actuator volume of each EPP can be found in table S1.

Outlying spikes in generated pressure were removed using MATLAB "medfilt1" function (default arguments), and noise was removed using the MATLAB smooth function with a span argument of 50 (calculating a smoothed value from 50 data points). Efficiency was also smoothed using the same approach. Examples of input and output energy, power, and efficiency of EPPs during pressure generation and the comparison between EPPs with four different designs are shown in figs. S7 and S8, respectively.

SUPPLEMENTARY MATERIALS

robotics.sciencemag.org/cgi/content/full/6/51/eabc3721/DC1
Materials and Methods
Fig. S1. Models used to derive electrostatic force in the EPP.
Fig. S2. Flowchart showing structure of a recursive MATLAB script for the EPP model.
Fig. S3. Results from the EPP simulation.
Fig. S4. Capability of the EPP (D1) in generating pressure.
Fig. S5. Experimental setup.
Fig. S6. Actuation of BAM.
Fig. S7. Pressure, input/output energy, power, and efficiency of EPP (D4) from pressure-generating evaluation.
Fig. S8. Comparison of energy, power, and efficiency of four EPPs with different designs (D1 to D4).
Fig. S9. Flow rate and pressure of the EPP pump (D1).
Fig. S10. Pressure generation of the bent EPP (D1).
Table S1. Design detail of four fabricated EPPs.
Movie S1. Actuation of a pneumatic artificial muscle by an EPP.
Movie S2. Zipping behavior of an EPP-BAM system with different injected air volumes.
Movie S3. EPP actuation speed for different applied voltages.
Movie S4. An EPP-BAM system at different frequencies.
Movie S5. Voltage control of the EPP-BAM system.
Movie S6. Antagonistic coupling of two EPP-BAM systems.
Movie S7. Arm-flexing robotic device.
Movie S8. EPP-driven continuous-pumping system.

REFERENCES AND NOTES

1. S. Kim, C. Laschi, B. Trimmer, Soft robotics: A bioinspired evolution in robotics. *Trends Biotechnol.* **31**, 287–294 (2013).
2. C. Laschi, B. Mazzolai, M. Cianchetti, Soft robotics: Technologies and systems pushing the boundaries of robot abilities. *Sci. Robot.* **1**, eaah3690 (2016).
3. D. Rus, M. T. Tolley, Design, fabrication and control of soft robots. *Nature* **521**, 467–475 (2015).
4. F. Daerden, D. Lefeber, Pneumatic artificial muscles: Actuators for robotics and automation. *Eur. J. Mech. Environ. Eng.* **47**, 11–21 (2002).
5. R. S. Diteesawat, T. Helps, M. Taghavi, J. Rossiter, Characteristic analysis and design optimization of bubble artificial muscles. *Soft Robot.*, (2020).
6. R. S. Diteesawat, T. Helps, M. Taghavi, J. Rossiter, High strength bubble artificial muscles for walking assistance, in *IEEE International Conference on Soft Robotics (RoboSoft)* (IEEE, 2018), pp. 388–393.
7. J. D. Greer, T. K. Morimoto, A. M. Okamura, E. W. Hawkes, Series pneumatic artificial muscles (sPAMs) and application to a soft continuum robot, in *IEEE International Conference on Robotics and Automation (ICRA)* (IEEE, 2017), pp. 5503–5510.
8. S. Kurumaya, H. Nabae, G. Endo, K. Suzumori, Design of thin McKibben muscle and multifilament structure. *Sens. Actuat. A Phys.* **261**, 66–74 (2017).
9. F. Daerden, D. Lefeber, The concept and design of pleated pneumatic artificial muscles. *Int. J. Fluid Power* **2**, 41–50 (2001).
10. R. Niiyama, D. Rus, S. Kim, Pouch motors: Printable/inflatable soft actuators for robotics, in *IEEE International Conference on Robotics and Automation (ICRA)* (IEEE, 2014), pp. 6332–6337.
11. M. A. M. Dzahir, S.-i. Yamamoto, Recent trends in lower-limb robotic rehabilitation orthosis: Control scheme and strategy for pneumatic muscle actuated gait trainers. *Robotics* **3**, 120–148 (2014).
12. M. Wehner, B. Quinlivan, P. M. Aubin, E. Martinez-Villalpando, M. Baumann, L. Stirling, K. Holt, R. Wood, C. Walsh, A lightweight soft exosuit for gait assistance, in *IEEE International Conference on Robotics and Automation* (IEEE, 2013), pp. 3362–3369.
13. T. Abe, S. Koizumi, H. Nabae, G. Endo, K. Suzumori, Muscle textile to implement soft suit to shift balancing posture of the body, in *IEEE International Conference on Soft Robotics (RoboSoft)* (IEEE, 2018), pp. 572–578.
14. Y.-L. Park, B.-r. Chen, C. Majidi, R. J. Wood, R. Nagpal, E. Goldfield, Active modular elastomer sleeve for soft wearable assistance robots, in *IEEE/RSJ International Conference on Intelligent Robots and Systems* (IEEE, 2012), pp. 1595–1602.
15. Y.-L. Park, J. Santos, K. G. Galloway, E. C. Goldfield, R. J. Wood, A soft wearable robotic device for active knee motions using flat pneumatic artificial muscles, in *IEEE International Conference on Robotics and Automation (ICRA)* (IEEE, 2014), pp. 4805–4810.
16. F. Ilievski, A. D. Mazzeo, R. F. Shepherd, X. Chen, G. M. Whitesides, Soft robotics for chemists. *Angew. Chem. Int. Ed.* **50**, 1890–1895 (2011).
17. Y. Hao, Z. Gong, Z. Xie, S. Guan, X. Yang, Z. Ren, T. Wang, L. Wen, Universal soft pneumatic robotic gripper with variable effective length, in *2016 35th Chinese Control Conference (CCC)* (IEEE, 2016), pp. 6109–6114.
18. M. Cianchetti, T. Ranzani, G. Gerboni, T. Nanayakkara, K. Althoefer, P. Dasgupta, A. Menciassi, Soft robotics technologies to address shortcomings in today's minimally invasive surgery: The STIFF-FLOP approach. *Soft Robot.* **1**, 122–131 (2014).
19. P. Ohta, L. Valle, J. King, K. Low, J. Yi, C. G. Atkeson, Y.-L. Park, Design of a lightweight soft robotic arm using pneumatic artificial muscles and inflatable sleeves. *Soft Robot.* **5**, 204–215 (2018).
20. J. W. Booth, D. Shah, J. C. Case, E. L. White, M. C. Yuen, O. Cyr-Choiniere, R. Kramer-Bottiglio, OmniSkins: Robotic skins that turn inanimate objects into multifunctional robots. *Sci. Robot.* **3**, eaat1853 (2018).

21. B. Shih, D. Shah, J. Li, T. G. Thuruthel, Y.-L. Park, F. Iida, Z. Bao, R. Kramer-Bottiglio, M. T. Tolley, Electronic skins and machine learning for intelligent soft robots. *Sci. Robot.* **5**, eaaz9239 (2020).
22. R. F. Shepherd, F. Ilievski, W. Choi, S. A. Morin, A. A. Stokes, A. D. Mazzeo, X. Chen, M. Wang, G. M. Whitesides, Multigait soft robot. *Proc. Natl. Acad. Sci. U.S.A.* **108**, 20400–20403 (2011).
23. E. W. Hawkes, L. H. Blumenschein, J. D. Greer, A. M. Okamura, A soft robot that navigates its environment through growth. *Sci. Robot.* **2**, eaan3028 (2017).
24. M. Wehner, R. L. Truby, D. J. Fitzgerald, B. Mosadegh, G. M. Whitesides, J. A. Lewis, R. J. Wood, An integrated design and fabrication strategy for entirely soft, autonomous robots. *Nature* **536**, 451–455 (2016).
25. M. Wehner, M. T. Tolley, Y. Mengüç, Y.-L. Park, A. Mozeika, Y. Ding, C. Onal, R. F. Shepherd, G. M. Whitesides, R. J. Wood, Pneumatic energy sources for autonomous and wearable soft robotics. *Soft Robot.* **1**, 263–274 (2014).
26. J. Zhang, J. Sheng, C. T. O'Neill, C. J. Walsh, R. J. Wood, J.-H. Ryu, J. P. Desai, M. C. Yip, Robotic artificial muscles: Current progress and future perspectives. *IEEE Trans. Robot.* **35**, 761–781 (2019).
27. S. M. Mirvakili, I. W. Hunter, Artificial muscles: Mechanisms, applications, and challenges. *Adv. Mater.* **30**, 1704407 (2018).
28. W. Huo, S. Mohammed, J. C. Moreno, Y. Amirat, Lower limb wearable robots for assistance and rehabilitation: A state of the art. *IEEE Syst. J.* **10**, 1068–1081 (2016).
29. C. Cao, X. Gao, A. T. Conn, A magnetically coupled dielectric elastomer pump for soft robotics. *Adv. Mater. Technol.* **4**, 1900128 (2019).
30. J. J. Loverich, I. Kanno, H. Kotera, Concepts for a new class of all-polymer micropumps. *Lab Chip* **6**, 1147–1154 (2006).
31. Z. Li, Y. Wang, C. C. Foo, H. Godaba, J. Zhu, C. H. Yap, The mechanism for large-volume fluid pumping via reversible snap-through of dielectric elastomer. *J. Appl. Phys.* **122**, 084503 (2017).
32. V. Cacucciolo, J. Shintake, Y. Kuwajima, S. Maeda, D. Floreano, H. Shea, Stretchable pumps for soft machines. *Nature* **572**, 516–519 (2019).
33. C. Stergiopulos, D. Vogt, M. T. Tolley, M. Wehner, J. Barber, G. M. Whitesides, R. J. Wood, A soft combustion-driven pump for soft robots, in *Volume 2: Mechanics and Behavior of Active Materials; Integrated System Design and Implementation; Bioinspired Smart Materials and Systems; Energy Harvesting* (American Society of Mechanical Engineers, 2014), pp. 1–6.
34. M. Garrad, G. Soter, A. T. Conn, H. Hauser, J. Rossiter, Driving soft robots with low-boiling point fluids, in *IEEE International Conference on Soft Robotics (RoboSoft)* (IEEE, 2019), pp. 74–79.
35. M. Taghavi, T. Helps, J. Rossiter, Electro-ribbon actuators and electro-origami robots. *Sci. Robot.* **3**, eaau9795 (2018).
36. E. Acome, S. K. Mitchell, T. G. Morrissey, M. B. Emmett, C. Benjamin, M. King, M. Radakovitz, C. Keplinger, Hydraulically amplified self-healing electrostatic actuators with muscle-like performance. *Science* **359**, 61–65 (2018).
37. S. K. Mitchell, X. Wang, E. Acome, T. Martin, K. Ly, N. Kellaris, V. G. Venkata, C. Keplinger, An easy-to-implement toolkit to create versatile and high-performance HASEL actuators for untethered soft robots. *Adv. Sci.* **6**, 1900178 (2019).
38. N. Kellaris, V. G. Venkata, G. M. Smith, S. K. Mitchell, C. Keplinger, Peano-HASEL actuators: Muscle-mimetic, electrohydraulic transducers that linearly contract on activation. *Sci. Robot.* **3**, eaar3276 (2018).
39. MGD 1000S specification; https://www.micropumps.co.uk/TCSMGD1000range.htm.
40. V. Cacucciolo, H. Nabae, K. Suzumori, H. Shea, Electrically-driven soft fluidic actuators combining stretchable pumps with thin McKibben muscles. *Front. Robot. AI* **6**, 146 (2020).
41. S. Pourazadi, A. Shagerdmootaab, H. Chan, M. Moallem, C. Menon, On the electrical safety of dielectric elastomer actuators in proximity to the human body. *Smart Mater. Struct.* **26**, 115007 (2017).
42. S. Bluett, T. Helps, M. Taghavi, J. Rossiter, Self-sensing electro-ribbon actuators. *IEEE Robot. Autom. Lett.* **5**, 3931–3936 (2020).
43. R. S. Diteesawat, A. Fishman, T. Helps, M. Taghavi, J. Rossiter, Closed-loop control of electro-ribbon actuators. *Front. Robot. AI* **7**, 10.3389/frobt.2020.557624 (2020).
44. M. Taghavi, T. Helps, J. Rossiter, Characterisation of self-locking high-contraction electro-ribbon actuators, in *IEEE International Conference on Intelligent Robots and Systems* (IEEE, 2020), pp. 5856–5861.

Funding: R.S.D. was supported by the Engineering and Physical Sciences Research Council (EPSRC) through grants EP/L015293/1 and EP/S026096/1. T.H. was supported by the Royal Academy of Engineering and the Office of the Chief Science Adviser for National Security under the UK Intelligence Community Postdoctoral Fellowship Programme. M.T. was supported by EPSRC grant EP/R02961X/1. J.R. was supported by EPSRC grants EP/L015293/1, EP/M020460/1, EP/R02961X/1, and EP/S026096/1; the Royal Academy of Engineering through the Chair in Emerging Technologies scheme; and Royal Society - ERA Foundation Translation Award TA\R1\170060. **Author contributions:** R.S.D., T.H., M.T., and J.R. jointly conceived EPPs and all device concepts. R.S.D. designed the experiments, manufactured the devices, collected the data, performed the analysis, interpreted the results, wrote the manuscript, and created the movies. T.H., M.T., and J.R. advised on all parts of the project and reviewed and edited the manuscript. **Competing interests:** R.S.D. has no competing interests. Two patent applications have been filed relating to this work by the University of Bristol: GB1710400.1A and WO2019002860A1 (inventors: T.H., M.T., and J.R.). **Data and materials availability:** All data needed to evaluate the conclusions in the paper are present in the paper or in the Supplementary Materials. The datasets generated and analyzed during the current study are available in the University of Bristol Research Data Repository (https://data.bris.ac.uk/data): https://doi.org/10.5523/bris.2v49dy7vowv8924ryb4dyd115p.

Submitted 23 April 2020
Accepted 19 January 2021
Published 17 February 2021
10.1126/scirobotics.abc3721

Citation: R. S. Diteesawat, T. Helps, M. Taghavi, J. Rossiter, Electro-pneumatic pumps for soft robotics. *Sci. Robot.* **6**, eabc3721 (2021).

Science Robotics

Electro-pneumatic pumps for soft robotics

R. S. Diteesawat, T. Helps, M. Taghavi, and J. Rossiter

Sci. Robot. **6** (51), eabc3721. DOI: 10.1126/scirobotics.abc3721

Science Robotics (ISSN 2470-9476) is published by the American Association for the Advancement of Science. 1200 New York Avenue NW, Washington, DC 20005. The title *Science Robotics* is a registered trademark of AAAS.